Synthesis of virtual monoenergetic images from kilovoltage peak images using wavelet loss enhanced CycleGAN for improving radiomics features reproducibility

Zilong Xu[1,2], Miaomiao Li[3], Baosheng Li[1,2], Huazhong Shu[1]

[1]Laboratory of Image Science and Technology, School of Computer Science and Engineering, Southeast University, Nanjing, China; [2]Department of Radiation Oncology, Shandong Cancer Hospital and Institute, Shandong First Medical University and Shandong Academy of Medical Sciences, Jinan, China; [3]Department of Medical Image, Shandong Medical College, Jinan, China

Contributions: (I) Conception and design: Z Xu; (II) Administrative support: B Li, H Shu; (III) Provision of study materials or patients: M Li; (IV) Collection and assembly of data: M Li; (V) Data analysis and interpretation: Z Xu; (VI) Manuscript writing: All authors; (VII) Final approval of manuscript: All authors.

Correspondence to: Baosheng Li, PhD. Laboratory of Image Science and Technology, School of Computer Science and Engineering, Southeast University, 2 Sipailou Road, Xuanwu District, Nanjing 210096, China; Department of Radiation Oncology, Shandong Cancer Hospital and Institute, Shandong First Medical University and Shandong Academy of Medical Sciences, Jinan, China. Email: bsli@sdfmu.edu.cn; Huazhong Shu, PhD. Laboratory of Image Science and Technology, School of Computer Science and Engineering, Southeast University, 2 Sipailou Road, Xuanwu District, Nanjing 210096, China. Email: shu.list@seu.edu.cn.

Background: Dual-energy computed tomography (CT) can provide a range of image information beyond conventional CT through virtual monoenergetic images (VMIs). The purpose of this study was to investigate the impact of material decomposition in detector-based spectral CT on radiomics features and effectiveness of using deep learning-based image synthesis to improve the reproducibility of radiomics features.

Methods: In this paper, spectral CT image data from 45 esophageal cancer patients were collected for investigation retrospectively. First, we computed the correlation coefficient of radiomics features between conventional kilovoltage peak (kVp) CT images and VMI. Then, a wavelet loss-enhanced CycleGAN (WLL-CycleGAN) with paired loss terms was developed to synthesize virtual monoenergetic CT images from the corresponding conventional single-energy CT (SECT) images for improving radiomics reproducibility. Finally, the radiomic features in 6 different categories, including gray-level co-occurrence matrix (GLCM), gray-level difference matrix (GLDM), gray-level run-length matrix (GLRLM), gray-level size-zone matrix (GLSZM), neighborhood gray-tone difference matrix (NGTDM), and wavelet, were extracted from the gross tumor volumes from conventional single energy CT, synthetic virtual monoenergetic CT images, and virtual monoenergetic CT images. Comparison between errors in the VMI and synthetic VMI (sVMI) suggested that the performance of our proposed deep learning method improved the radiomic feature accuracy.

Results: Material decomposition of dual-layer dual-energy CT (DECT) can substantially influence the reproducibility of the radiomic features, and the degree of impact is feature dependent. The average reduction of radiomics errors for 15 patients in testing sets was 96.9% for first-order, 12.1% for GLCM, 12.9% for GLDM, 15.7% for GLRLM, 50.3% for GLSZM, 53.4% for NGTDM, and 6% for wavelet features.

Conclusions: The work revealed that material decomposition has a significant effect on the radiomic feature values. The deep learning-based method reduced the influence of material decomposition in VMIs and might improve the robustness and reproducibility of radiomic features in esophageal cancer. Quantitative results demonstrated that our proposed wavelet loss-enhanced paired CycleGAN outperforms the original CycleGAN.

Introduction

Radiomics has been applied to extract information from image data as biomarkers for outcome prediction and treatment assessment (1-3). Morphological, intensity-based, textural features, and wavelets features can be extracted and assessed to uncover imaging patterns exceeding the ordinary visual image interpretation by the naked eye (1,4).

In recent years, due to the widespread applications of deep learning in the field of medical imaging, the latest achievements have been incorporated into medical image synthesis and translation involving computed tomography (CT). These works were categorized into 2 main groups: synthesis of CT from other modalities (5-8) and intra-modality synthesis (9-11). Many works have indicated that image quality or construction configuration have a significant influence on radiomic feature values (12,13). The reproducibility of radiomics is sensitive to scanning parameters such as kilovoltage (kV), tube current (mAs), slice thickness, spatial resolution, and image reconstruction algorithm. The standardization of imaging protocols is a solution to overcome the challenge of reproducibility in radiomics (13). However, this idea requires more manual intervention and has not yet provided widely-used guidelines for the clinical applications of scanning protocols. Recently, several works have suggested the promising effectiveness of image synthesis or conversion through deep learning methods to improve the reproducibility and accuracy of radiomic features. A convolutional neural network (CNN) was employed to convert CT images with different reconstruction kernels for improving radiomics reproducibility (14). Generative adversarial networks (GAN) have been applied to standardize radiomics features extracted from images obtained from imaging devices produced by different manufacturers (15) or devices of different hospitals (16). The influence of 4-dimensional cone beam CT (4D-CBCT) image quality on radiomics has been investigated and the temporally coherent GANs for video super-resolution (TecoGAN) has been applied to enhance 4D-CBCT for improving radiomics accuracy (17). In addition, the impact of CT image slice thickness on the radiomic features' reproducibility has also been studied (18). A super-resolution approach based on a CNN model was proposed to synthesize the CT images with slice thickness of 1 mm from that of 3 and 5 mm.

Dual-energy CT (DECT), also known as spectral, multi-energy, or polychromatic CT, employs dual image acquisition at different kV levels of the same scan volume to enable material separation (19). Virtual monoenergetic images (VMIs) from DECT are incrementally used in routine clinical practice (20). Recently, DECT images have been used to produce imaging features for radiomics analysis in several publications (21,22). Due to the difference of reconstruction approaches and parameters, conventional CT images and VMI may have distinct pixel distributions. Distributions of pixels in various VMI may also differ from one another. The VMI produced by the DECT can provide different image contrasts: low energy (40–60 keV) for high soft tissue contrast and iodine attenuation; high energy (120–200 keV) to depress beam hardening and metal artifacts (23-25). Therefore, different levels of VMI obtained from 1 scan may provide different values of the same radiomics feature by DECT device. This facilitates the extraction of different dimensions of information from the same image, thus contributing to radiomics analysis. Existing DECT acquisition techniques include dual-source, fast voltage switching, dual-layer, and dual-spiral (25).

Several deep learning approaches have been employed to address VMI of DECT. ResNet was used to produce virtual monoenergetic CT from polyenergetic (single-spectrum) CT (26). Conditional generative adversarial networks (cGAN) can synthesize pseudo low monoenergetic CT images from a single-tube voltage CT scanner (27). Material decomposition in DECT from a kilovoltage CT could be performed through deep convolutional generative adversarial networks (DCGAN) (28). CNN has been used to estimate DECT images from single-energy CT (SECT) (29).

In this study, we compared radiomics feature reproducibility between ground-truth VMI, conventional SECT, and our generated synthetic VMI (sVMI). sVMIs were generated from SECT using our proposed wavelet

Table 1 Characteristics of study patients

Variables	Values (n=45)
Sex	
Men	37 (82.2)
Women	8 (17.8)
Age (years)	67.4±9.2
ROI volume (mm^3)	22.9±18.1
ROI surface area (mm^2)	53.5±28.0
Primary site	
Upper thoracic	16
Middle thoracic	23
Lower thoracic	11
Clinical stage	
II	4
III	38
IV	3
T stage	
T1	1
T2	4
T3	12
T4	28
N stage	
N0	15
N1	13
N2	16
N3	1
M stage	
M0	43
M1	2

Unless otherwise stated, data are the number of patients; data in parentheses are percentages. ROI, region of interest.

loss-enhanced CycleGAN approach and evaluated against ground-truth VMI for improvement in precision of radiomics analysis. Our main contributions of this work are the following:

(I) The impact of VMI on radiomics features was investigated. Radiomics feature values were extracted from the region of interest (ROI) of conventional CT images and VMIs. The concordance correlation coefficient was used to evaluate the difference.

(II) The CycleGAN model was employed to improve radiomics reproducibility against virtual mono energy. The conventional CT images were fed to the network and then monoenergetic images were synthesized.

(III) We defined the wavelet loss of 2 images to evaluate the high-frequency detailed differences. The proposed wavelet loss was incorporated into the CycleGAN model to enhance the synthesis performance.

Methods

Datasets

We retrospectively collected image data from 45 patients obtained using detector-based dual-layer DECT scanner of the IQon Spectral CT System (Philips Healthcare, Cleveland, OH, USA). For each patient, we obtained pretreatment VMIs at various energy levels and conventional CT images under the standard tube-voltage setting. The following CT protocols were used for all image acquisitions: tube voltage, 120 kilovoltage peak (kVp); slice thickness, 3 mm; pixel spacing, 0.8 mm; protocol name, Chest + ABD + C/Thorax. The collected data is described in *Table 1*.

The ROIs were segmented and delineated manually by the physician using the open-source medical image software 3D Slicer (version 4.10.2) (30).

VMIs are produced from the original projection images using the material decomposition algorithm. Therefore, VMIs at various keV levels and conventional CT images are pixel-wise corresponding for each patient and image registration is not required as a preprocessing operation.

The study was conducted in accordance with the Declaration of Helsinki (as revised in 2013). The study was approved by the Ethics Committee of Shandong Cancer Hospital and Institute, and the requirement for individual consent for this retrospective analysis was waived.

Deep learning system/pipeline

The basic purpose was to evaluate the effectiveness of deep learning model for improving feature reproducibility between VMIs (kVp images) and conventional CT images.
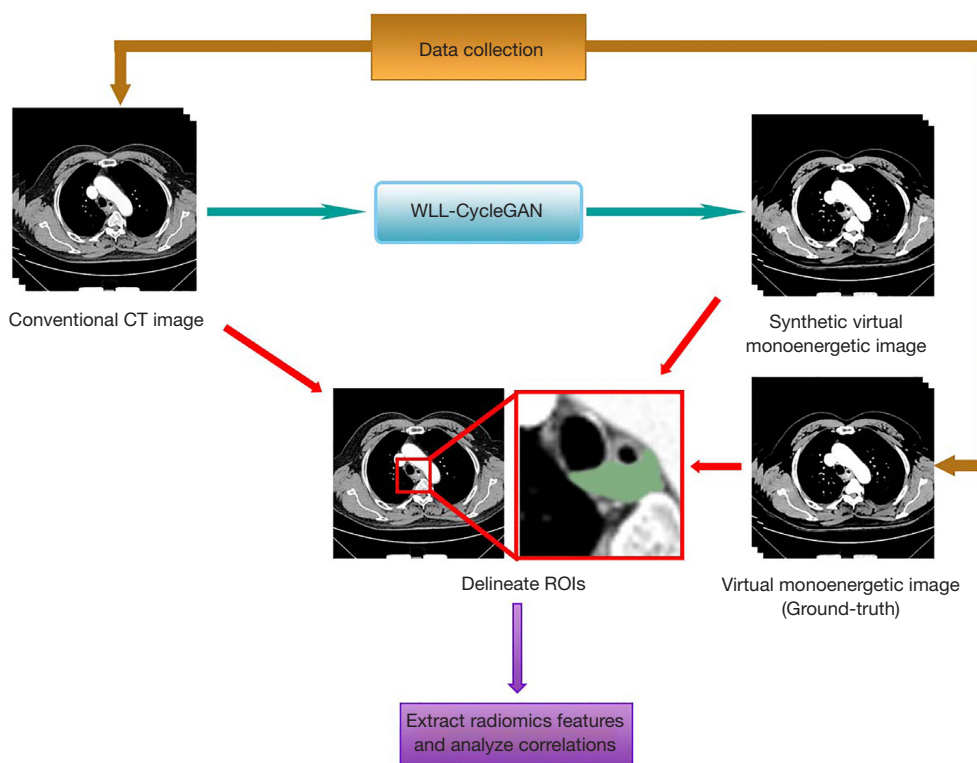
Figure 1 The workflow of the whole study. CT, computed tomography; WLL, wavelet loss; GAN, generative adversarial network; ROI, region of interest.

We trained the CycleGAN-based deep learning model to convert conventional CT images to VMIs, and vice versa.

The workflow of the study consists of 5 steps (see *Figure 1*):

(I) Data collection: acquire detector-based dual-layer spectral CT images including conventional kVp images and VMIs.

(II) The correlation coefficients of radiomics features between conventional CT images and VMIs at various energy levels were computed to investigate the impact of material decomposition in detector-based dual-energy spectral CT on radiomic features.

(III) Image conversion employing CycleGAN: conventional CT images were served as input, and the corresponding VMIs were served as output.

(IV) Radiomics extraction: radiomic features were extracted from the ROI of each patient.

(V) Performance evaluation: intensity histograms, difference image, and sVMIs were compared to radiomic features extracted from VMIs.

CycleGAN-based deep learning network

The network architecture

A classical GAN model uses the generator and discriminator networks competing with each other. In a study (31), researchers developed the CycleGAN model to perform translation in 2 directions between 2 image domains. In this work, we leveraged the CycleGAN with paired loss proposed in previous research (32,33) as our benchmark model to learn the mapping between images with different energetic configurations. Furthermore, we defined the wavelet loss of 2 images and the proposed wavelet loss item was incorporated into the benchmark model to enhance the effect.

Energy-spectrum CT images, including both conventional CT images and VMIs, are reconstructed from the same projection data acquired from a single scan (34). Unlike conventional CT images, the reconstruction process of VMIs requires material decomposition algorithms (35,36). There is a pixel-wise correspondence between a series of VMIs and conventional (kVp) images. Therefore,

paired data training is available in our work.

The cycle and synthesis loss

The total cycle and synthetic consistency loss function $L_{(cyc+syn)}$ used in the proposed model is represented as:

$$
\begin{aligned}
& L_{(cyc+syn)}\left(G_{con\text{-}VM}\left(I_{con}\right), G_{VM\text{-}con}\left(I_{VM}\right)\right) \\
& = \lambda_{MPL} MPL\left(G_{con\text{-}VM}\left(I_{con}\right), G_{VM\text{-}con}\left(I_{VM}\right)\right) \\
& \quad + \lambda_{GML} GML\left(G_{con\text{-}VM}\left(I_{con}\right), G_{VM\text{-}con}\left(I_{VM}\right)\right)
\end{aligned}
\tag{1}
$$

where $G_{con\text{-}VM}$ is the generator converting conventional CT images to VMIs, $G_{VM\text{-}con}$ denotes the generator converting VMIs to conventional CT images, I_{con} denotes conventional CT images, I_{VM} denotes VMIs, λ_{MPL} is the weighting coefficient of mean pixel loss (MPL), and λ_{GML} is the coefficient of gradient magnitude loss (GML) (32) item.

The losses in equation (1) are defined as follows:

$$
MPL\begin{pmatrix} G_{SECT\text{-}VMI}, \\ G_{VMI\text{-}SECT}, \\ I_{SECT}, I_{VMI} \end{pmatrix} = \frac{1}{N_{I_{SECT}}}\left\{ \lambda_{loss}^{cycle}\left[\begin{array}{l} \left\| G_{VMI\text{-}SECT}\left(G_{SECT\text{-}VMI}\right) - I_{SECT} \right\|_2^2 \\ + \left\| G_{SECT\text{-}VMI}\left(G_{VMI\text{-}SECT}\right) - I_{VMI} \right\|_2^2 \end{array} \right] + \lambda_{loss}^{syn}\left[\begin{array}{l} \left\| G_{VMI\text{-}SECT} - I_{SECT} \right\|_2^2 \\ + \left\| G_{SECT\text{-}VMI} - I_{VMI} \right\|_2^2 \end{array} \right] \right\}
\tag{2}
$$

$$
GML\begin{pmatrix} G_{VMI\text{-}SECT}, \\ G_{SECT\text{-}VMI}, \\ I_{SECT}, I_{VMI} \end{pmatrix} = \lambda_{dist}^{cyc}\left\{ \begin{array}{l} GMD\left[G_{VMI\text{-}SECT}\left(G_{SECT\text{-}VMI}\right), I_{SECT}\right] \\ + GMD\left[G_{SECT\text{-}VMI}\left(G_{VMI\text{-}SECT}\right), I_{VMI}\right] \end{array} \right\} + \lambda_{dist}^{syn}\left[\begin{array}{l} GMD\left(G_{VMI\text{-}SECT}, I_{SECT}\right) \\ + GMD\left(G_{SECT\text{-}VMI}, I_{VMI}\right) \end{array} \right]
\tag{3}
$$

where I_{con} is conventional CT images, I_{VM} is VMIs; gradient magnitude distance (GMD) (32) denotes the Euclidean distance of image gradients.

The wavelet loss

The wavelet domain images produced by wavelet transform can depict the details multi-level frequency components of the original images. We proposed the wavelet loss (WLL) to improve the performance of the model.

First of all, the sub bands are computed by the discrete wavelet transformation (DWT).

$$
SB(I) = \{A, V, H, D\} = 2dDWT(I)
\tag{4}
$$

where I denote the original image, A, V, H and D denote the sub-bands containing wavelet coefficients for average, vertical, horizontal, and diagonal details, respectively.

The wavelet loss between 2 images is defined as:

$$
\begin{aligned}
& WLL(I_r, I_s) = MSE\left(BatNor\left(SB_i(I_r), SB_i(I_s)\right)\right) \\
& i \in \{A, V, H, D\}
\end{aligned}
\tag{5}
$$

where I_r denotes the real image, I_s denotes the synthetic image, $SB_i(I_r)$ denotes the sub-brand of the real image, $SB_i(I_s)$ denotes the sub-brand of the synthetic image, *MSE* denotes the mean square error operator of 2 images, and *BatNor* is the batch normalization operator using the min-max method, defined as follows:

$$
(A', B') = Batnor(A, B)
\tag{6}
$$

where A and B are the images to be normalized, A' and B' are the normalized images. The normalization process including the following steps:

$$
p_{max} = \max\left\{\max(A), \ \max(B)\right\}
\tag{7}
$$

$$
p_{min} = \min\left\{\min(A), \ \min(B)\right\}
\tag{8}
$$

$$
A'_{i,j} = \frac{A_{i,j} - p_{min}}{p_{max} - p_{min}}
\tag{9}
$$

$$
B'_{i,j} = \frac{B_{i,j} - p_{min}}{p_{max} - p_{min}}
\tag{10}
$$

where p_{max} denotes the maximal pixel value of the 2 input images, p_{min} denotes the minimal pixel value of the 2 input images, and i and j denote the coordinates of the pixels in the image.

The computation of wavelet loss includes 5 steps:

(I)   Discrete wavelet transform is applied on the real images and synthetic images to generate 4 wavelet sub-bands images.

(II)   The images of the same sub-band are grouped in 1 group.

(III)   Normalization is performed on intragroup images in each group. Pixel values in different sub-bands groups have large difference. For optimizing loss from each sub-band uniformly, intragroup normalization is performed. Meanwhile, intragroup normalization can reserve the difference between the sub-bands image deduced from real and synthetic images.

(IV)   The mean square error is computed for normalized intragroup images.

(V)   The sum of all 4 sub-bands groups is obtained as the wavelet loss item. The overall process of obtaining
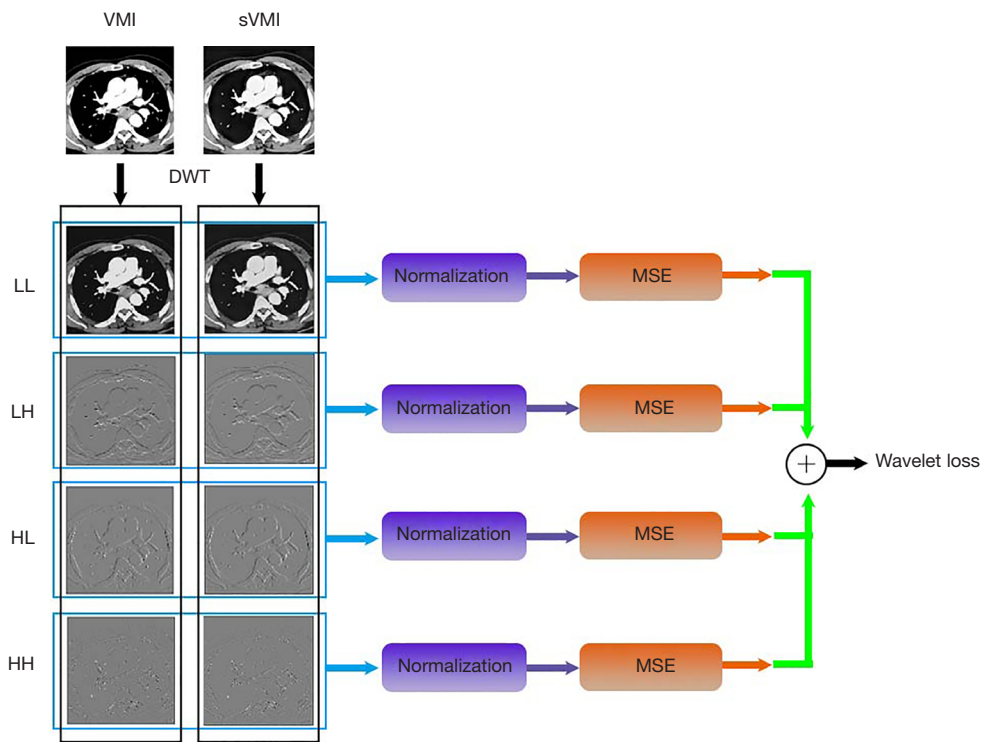
Figure 2 The workflow for computing the wavelet loss. VMI, virtual monoenergetic image; sVMI, synthetic virtual monoenergetic image; DWT, discrete wavelet transformation; LL, low pass filter for each row and column (average details); LH, low pass filter for each row and high pass filter for each column (vertical details); HL, high pass filter for each row and low pass filter for each column (horizontal details); HH, high pass filter for each row and column (diagonal details); MSE, mean square error; Normalization, min-max normalization is used in the framework.

WLL is revealed in *Figure 2*.

The wavelet loss is incorporated into the framework of synthetic consistency and cycle consistency.

$$
\begin{aligned}
WLL_{s+c} &= WLL_s + WLL_c \\
&= \begin{bmatrix} WLL\left(I_{VMI}, G_{SECT\text{-}VMI}\left(I_{SECT}\right)\right) \\ + WLL\left(I_{SECT}, G_{VMI\text{-}SECT}\left(I_{VMI}\right)\right) \end{bmatrix} \\
&+ \begin{bmatrix} WLL\left(I_{VMI}, G_{SECT\text{-}VMI}\left(G_{VMI\text{-}SECT}\left(I_{VMI}\right)\right)\right) \\ + WLL\left(I_{SECT}, G_{VMI\text{-}SECT}\left(G_{SECT\text{-}VMI}\left(I_{SECT}\right)\right)\right) \end{bmatrix}
\end{aligned}
\tag{11}
$$

where WLL_s denotes the synthetic consistency of WLL, WLL_c denotes the cycle consistency of WLL, and WLL_{s+c} denotes the sum of WLL_s and WLL_c.

The total cycle and synthetic consistency loss function in equation 1 will be extended to the new form as:

$$
\begin{aligned}
L_{(cyc+syn)}\left(G_{SECT\text{-}VMI}, G_{VMI\text{-}SECT}\right) &= \lambda_{MPL} MPL\left(G_{SECT\text{-}VMI}, G_{VMI\text{-}SECT}\right) \\
&+ \lambda_{GML} GML\left(G_{SECT\text{-}VMI}, G_{VMI\text{-}SECT}\right) \\
&+ \lambda_{WLL} WLL_{s+c}\left(G_{SECT\text{-}VMI}, G_{VMI\text{-}SECT}\right)
\end{aligned}
\tag{12}
$$

The adversarial loss

The adversarial loss function, depending on the output of the discriminators, applies to both the Con-to-VMI generator and the VMI-to-Con generator. The adversarial loss for both directions is represented as follows:

$$
\begin{aligned}
&L_{adv}\left(G_{SECT\text{-}VMI}, D_{VMI}, I_{SECT}, I_{VMI}\right) + L_{adv}\left(G_{VMI\text{-}SECT}, D_{SECT}, I_{VMI}, I_{SECT}\right) \\
&= MSE\left[D_{VMI}\left(G_{SECT\text{-}VMI}\left(I_{SECT}\right)\right), 1\right] + MSE\left[D_{VMI}\left(I_{VMI}\right)\right] \\
&+ MSE\left[D_{SECT}\left(G_{VMI\text{-}SECT}\left(I_{VMI}\right)\right), 1\right] + MSE\left[D_{SECT}\left(I_{SECT}\right)\right]
\end{aligned}
\tag{13}
$$

where MSE[•, 1] is the mean square error between the discriminator map of the sVMI and a unit mask.

The total loss

The total loss function of the model consists of the generator loss and the discriminator loss, defined as:

$$
\begin{aligned}
&L\left(G_{SECT\text{-}VMI}, G_{VMI\text{-}SECT}, D_{VMI}, D_{SECT}, I_{SECT}, I_{VMI}\right) \\
&= L_{adv}\left(G_{SECT\text{-}VMI}, D_{VMI}, I_{SECT}, I_{VMI}\right) \\
&+ L_{adv}\left(G_{VMI\text{-}SECT}, D_{SECT}, I_{VMI}, I_{SECT}\right) \\
&+ \lambda_{(cyc+syn)} L_{(cyc+syn)}\left(G_{SECT\text{-}VMI}, G_{VMI\text{-}SECT}, I_{SECT}, I_{VMI}\right)
\end{aligned}
\tag{14}
$$

2376

Xu et al. CycleGAN method for improving radiomics features robustness

Table 2 Settings for radiomic features extracted

Setting item	Value
Scanner type	IQon Spectral CT System (Vendor: Philips Healthcare, Cleveland)
Acquisition protocol	SD Chest + ABD + C/Thorax
Tube voltage, kVp	120
Tube current, mA	359
Pixel spacing, mm	0.86
Image slice thickness, mm	3
Convolution kernel	B
Exposure, ms	493
Interpolation method	BSpline
Discretization: width of the bins, gray level	25
CM symmetry	Symmetry
CM distance, pixel	1
SZM linkage distance, pixel	1
NGTDM distance, pixel	1
Software availability	PyRadiomics version: 3.0.1

CM, co-occurrence matrix; SZM, size-zone matrix; NGTDM, neighborhood gray-tone difference matrix; kVp, kilovoltage peak.

where $\lambda_{(cyc+syn)}$ is the coefficient of the cycle and synthetic consistency loss. We aim to solve:

$$G^*_{SECT\text{-}VMI}, G^*_{VMI\text{-}SECT}, D^*_{VMI}, D^*_{SECT}$$
$$= \arg \min_{\substack{G_{SECT\text{-}VMI} \\ G_{VMI\text{-}SECT}}} \max_{\substack{D_{VMI} \\ D_{SECT}}} L\left(G_{SECT\text{-}VMI}, G_{VMI\text{-}SECT}, D_{VMI}, D_{SECT}\right) \qquad [15]$$

$G_{\text{SECT-VMI}}$, $G_{\text{VMI-SECT}}$ are updated to minimize this objective, whereas D_{VMI}, D_{SECT} attempt to maximize it.

Implementation and configuration of parameters

The model was implemented in Python 3.6 (37) and Tensorflow r1.3 (38) framework. The version of used CUDA was 10.0.

Hyperparameter values in the loss function were set as 10 for λ^{cyc}_{loss}, 1 for λ^{syn}_{loss}, 1 for λ^{syn}_{dist}, 1 for λ^{cyc}_{dist}, 1 for λ_{MPL}, 1 for λ_{GML}, 1 for λ_{WLL}, and 1 for $\lambda_{(cyc+syn)}$. The initial learning rate was set to be 0.0002 for both the generator and the descriminator. The Adam optimizer with beta1=0.5 and beta2=0.999 was employed to optimize both the generator and the descriminator.

Experiment design

Radiomics feature extraction

In this study, radiomics extraction included 4 steps: (I)

collect the images; (II) delineate and segment the ROIs; (III) preprocessing; (IV) feature extraction.

All radiomics features were extracted using the PyRadiomics package (39). For each patient, conventional CT images and various VMIs were reconstructed and obtained. The extracted features included 18 first order features, 22 gray-level co-occurrence matrix (GLCM) features (40), 14 gray-level difference matrix (GLDM) features, 16 gray-level run-length matrix (GLRLM) features (41), 16 gray-level size-zone matrix (GLSZM) features (42), and 5 neighborhood gray-tone difference matrix (NGTDM) features (43). Since ROI contour in various monoenergetic images for each patient is the same, the shape features were not considered. The settings of imaging for radiomics extraction are listed as *Table 2*.

Figure 3 shows the concordance correlation coefficient between conventional CT images and different VMIs. Each cell represents the concordance correlation coefficient between radiomics features of conventional CT images and VMIs.

Evaluation metrics

Our proposed method was compared with the pix2pix (44) model and the CycleGAN model using several evaluation metrics. After training, we evaluated the performance of
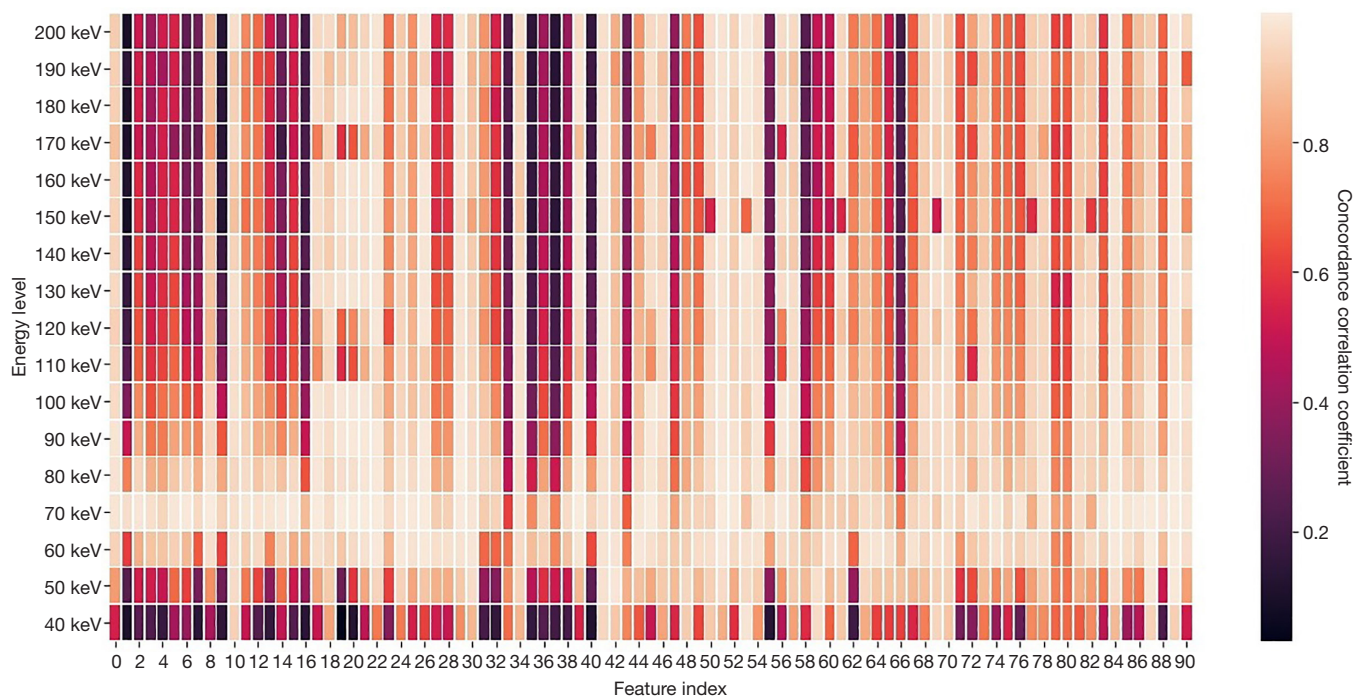
Figure 3 Correlation between conventional CT images (i.e., conventional 120 kVp image) and different VMIs. Each cell represents the concordance correlation coefficient between radiomics features of conventional CT images and VMIs. CT, computed tomography; kVp, kilovoltage peak; VMIs, virtual monoenergetic images.

the model through comparing the radiomics feature values extracted of synthetic images and source images. The first order, GLCM, GLDM, GLRLM, GLSZM, NGTDM, and wavelet from the whole body and ROI of conventional CT images, VMIs, and synthetic virtual monoenergetic CT images were compared.

For quantitative evaluation, the error of each feature was defined as:

$$Error = \frac{\left|Synthetic\ image\ feature - Groundtruth\ image\ feature\right|}{\left|Groundtruth\ image\ feature\right|} \quad [16]$$

The concordance correlation coefficient (CCC) was defined as:

$$C = \frac{2\rho\sigma_x\sigma_y}{\sigma_x^2 + \sigma_y^2 + \left(\mu_x - \mu_y\right)^2} \quad [17]$$

where μ_x and μ_y are the means for the two variables and σ_x^2 and σ_y^2 are the corresponding variances. ρ is the correlation coefficient between the 2 variables.

Results

Image evaluation

Conventional CT image, synthetic 40 keV VMI s, and 40 keV monoenergetic images are displayed in *Figure 4*. The results indicate that the CycleGAN model can synthesize approximately 40 keV monoenergetic images with high contrast and less streak artifacts from corresponding conventional kVp images. The difference images of conventional CT image versus 40 keV image and synthetic 40 keV image versus 40 keV image are displayed in *Figure 5*. The top line shows the result of the whole body, whereas the bottom line shows the result of the ROI of the tumor. These results suggests that the deep learning model converts original conventional CT image pixel values to 40 keV pixel values in both ROI and whole body accurately.

Standard evaluation measures were produced for image quality comparison with within ROIs and entire body contour. The results, including the mean values and standard deviations of measures, were shown in *Table 3*
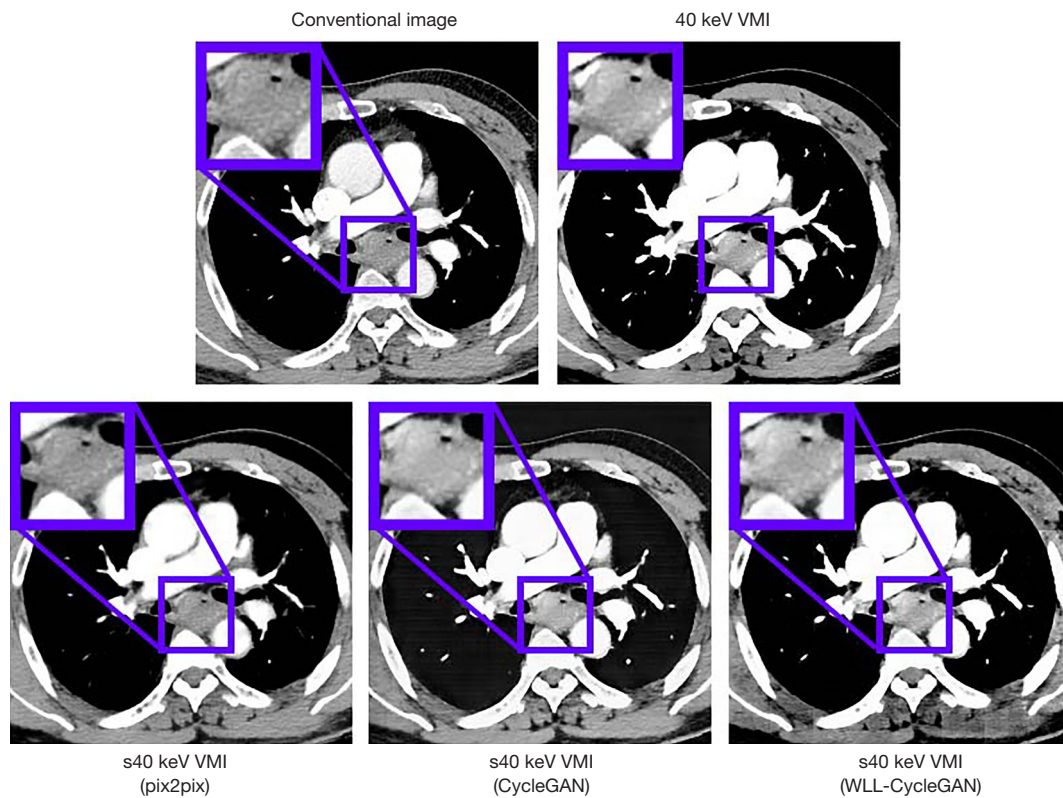
Figure 4 Image and ROI comparison: top row, column 1: conventional CT image; top row, column 2: 40 keV VMI; bottom row, column 1: synthetic 40 keV virtual monoenergetic image via pix2pix model; bottom row, column 2: synthetic 40 keV virtual monoenergetic image via CycleGAN; bottom row, column 3: synthetic 40 keV virtual monoenergetic image via proposed WLL-CycleGAN. All images are from the same slice of one patient. VMI, virtual monoenergetic image; s40 keV VMI, synthetic 40 keV VMI; GAN, generative adversarial network; WLL, wavelet loss; ROI, region of interest; CT, computed tomography.

and *Table 4*. The synthetic 40 keV VMIs generated from the 120 kVp conventional CT images using the proposed CycleGAN-based method were similar to the 40-keV VMIs obtained from the DECT device. Our proposed wavelet loss enhancement significantly improved the quality of the VMIs synthesized by the CycleGAN model.

The line intensity histograms of conventional CT images, VMI, and sVMIs using various methods are shown in *Figure 6*. The results suggested that the CycleGAN model can calibrate the Hounsfield unit (HU) values distribution in conventional CT images nearing that of actual 40 keV monoenergetic images. The CT HU distribution of VMI synthesized by the proposed method closely reflects the actual VMI. The histogram line of our method is closer to that of the 40 keV VMI than other methods.

Quantitative evaluation for the comparison of histograms was also produced. We used the root mean square error to evaluate the difference between 2 histograms. The results (*Table 5*) indicated that the proposed method produced the best effect among all models to improve the reproducibility of radiomics features.

Radiomics evaluations

The results of CCC passing rate comparison are shown in *Table 6*. Alternative CCC thresholds were configured as 0.8 and 0.85. The proposed WLL-CycleGAN produced the best results in 4 feature classes (GLCM, GLDM, GLRLM, and wavelet) at both thresholds, whereas CycleGAN obtained the best result in GLSZM at both thresholds and in the first-order feature class at a threshold of 0.85. The heatmap for CCC passing rate comparison is shown in *Figure 7*. The results suggest that our proposed WLL-CycleGAN outperforms other models.

The comparisons of feature value error were revealed in
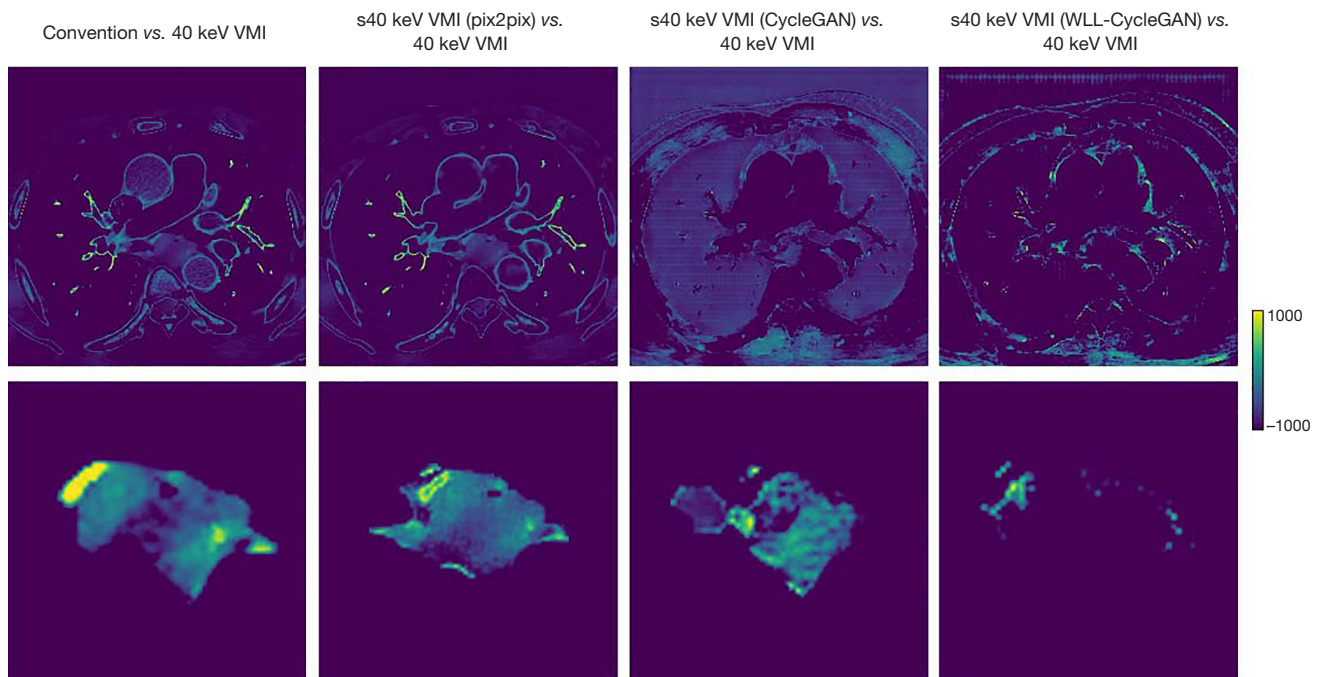
Figure 5 Image difference comparison among all methods. The images represent the distinction between synthetic virtual monoenergetic images and the virtual monoenergetic image. Top row: whole body comparison; bottom row: ROI comparison. Column 1: the difference between conventional CT images and 40 keV VMI. Column 2: the difference between synthetic 40 keV VMIs using pix2pix model and VMIs. Column 3: the difference between synthetic 40 keV VMIs using CycleGAN and 40 keV VMIs. Column 4: the difference between synthetic 40 keV VMIs using proposed WLL-CycleGAN and 40 keV VMIs. VMI, virtual monoenergetic image; s40 keV VMI, synthetic 40 keV VMI; GAN, generative adversarial network; WLL, wavelet loss; ROI, region of interest; CT, computed tomography.

Table 3 Image comparison (region of interest) with standard evaluation measures (from conventional CT image to 40 keV VMI)

| Comparison item	RMSE	PSNR	SSIM
Conv image *vs.* 40 keV	54.75±11.9	12.94±2.1	0.625±8.3
s40 keV (pix2pix) *vs.* 40 keV	43.61±6.1	13.58±1.1	0.716±4.5
s40 keV (CycleGAN) *vs.* 40 keV	38.46±4.8	30.41±1.1	0.831±2.6
s40 keV (WLL-CycleGAN) *vs.* 40 keV	32.03±4.7	32.03±1.4	0.906±3.1

Data format: mean ± standard deviation. CT, computed tomography; VMI, virtual monoenergetic CT images; RMSE, root mean square error; PSNR, peak signal-to-noise ratio; SSIM, structure similarity index measure; s40 keV, synthetic 40 keV; GAN, generative adversarial network; WLL, wavelet loss.

Table 4 Image comparison (entire body contour) with standard evaluation measures (from conventional CT image to 40 keV VMI)

Comparison item	RMSE	PSNR	SSIM
Conv image *vs.* 40 keV	92.67±36.1	23.78±4.9	0.994±0.1
s40 keV (pix2pix) *vs.* 40 keV	36.74±3.5	30.77±0.8	0.997±0.2
s40 keV (CycleGAN) *vs.* 40 keV	23.12±1.3	34.77±0.5	0.998±0.1
s40 keV (WLL-CycleGAN) *vs.* 40 keV	21.90±0.7	35.23±0.3	0.999±0.1

Data format: mean ± standard deviation. CT, computed tomography; VMI, virtual monoenergetic CT images; RMSE, root mean square error; PSNR, peak signal-to-noise ratio; SSIM, structure similarity index measure; s40 keV, synthetic 40 keV; GAN, generative adversarial network; WLL, wavelet loss.

tables and figures. *Figure 8* represents the error comparison of low-level texture features and *Figure 9* represents error comparison of wavelet-based features. The magnitude of the errors is significantly dependent on the feature. The results of various methods including pix2pix, CycleGAN, and proposed WLL-CycleGAN are displayed in these figures.
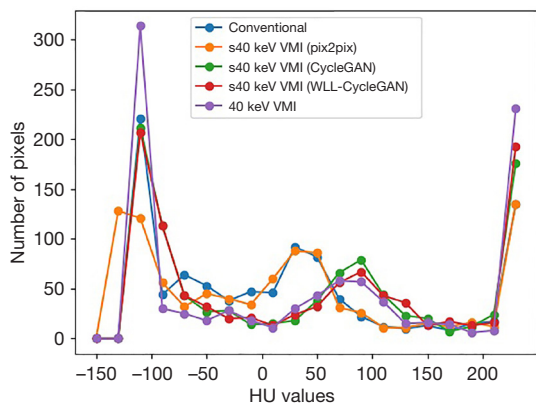
Figure 6 Histograms of HU values for each case for comparison. s40 keV VMI, synthetic 40 keV VMI; VMI, virtual monoenergetic image; WLL, wavelet loss; HU, Hounsfield unit.

Evaluations for the conversion from conventional CT image to VMIs

Inverse conversion, which involves synthesizing conventional CT images from VMIs, was also conducted in this work. The same image evaluation and radiomics feature evaluation were employed in this scheme.

The standard image evaluations of results of different methods were shown in several tables and figures. Image comparisons with standard evaluation measures are displayed in *Table 7*. Image and ROI comparison are displayed in *Figure 10*. *Figure 11* shows the image difference comparison among all methods. Histograms of HU values for each case for comparison are displayed in *Figure 12* and *Table 8* shows the quantitively metrics of the intensity histogram.

The radiomics evaluations are also represented in tables and figures. *Figure 13* represents the error comparison of low-level texture features, whereas *Figure 14* represents the comparison of wavelet-based features. *Table 9* shows the CCC passing rate comparison among methods. The proposed WLL-CycleGAN produced the best results in 3 feature classes (first order, GLCM, and GLSZM) at both thresholds, whereas CycleGAN obtained the best result

**Table 5** Quantitative metrics of intensity histogram

	Conventional *vs.* VMI	s40 keV VMI pix2pix	s40 keV VMI CycleGAN	s40 keV VMI WLL-CycleGAN
RMSE	58.59	83.49	28.59	28.32

GAN, generative adversarial network; s40 keV VMI, synthetic 40 keV virtual monoenergetic image; WLL, wavelet loss; RMSE, root mean square errors.

Table 6 Number of radiomic features meeting criteria of reproducibility before and after image conversion

Feature class	Conv-40 keV		40 keV-s40 keV (pix2pix)		40 keV-s40 keV (CycleGAN)		40 keV-s40 keV (WLL-CycleGAN)	
	0.8	0.85	0.8	0.85	0.8	0.85	0.8	0.85
First order	1 [5.6]	1 [5.6]	3 [16.7]	1 [5.6]	6 [33.3]	4 [22]	6 [33.3]	2 [11.1]
GLCM	2 [9]	2 [9]	3 [13.6]	1 [4.5]	7 [31.8]	3 [13]	9 [40.9]	8 [36.4]
GLDM	2 [14.3]	2 [14.3]	0 [0]	0 [0]	5 [35.7]	4 [28.6]	7 [50]	7 [50]
GLRLM	8 [50]	5 [31.2]	0 [0]	0 [0]	6 [37.5]	5 [31.2]	8 [50]	7 [43.8]
GLSZM	4 [25]	3 [18.8]	5 [31.25]	3 [18.8]	7 [43.8]	4 [25]	4 [25]	3 [18.8]
NGTDM	0 [0]	0 [0]	0 [0]	0 [0]	1 [20]	1 [20]	1 [20]	1 [20]
Wavelet	268 [36.8]	225 [31]	130 [17.9]	123[16.9]	274 [37.6]	203 [27.9]	324 [44.5]	277 [38]

(I) Numbers are count of radiomic features. Numbers in square brackets are percentages; (II) CCC are used as thresholds. s40 keV, synthetic 40 keV; GAN, generative adversarial network; WLL, wavelet loss; GLCM, gray-level co-occurrence matrix; GLDM, gray-level difference matrix; GLRLM, gray-level run-length matrix; GLSZM, gray-level size-zone matrix; NGTDM, neighborhood gray-tone difference matrix; CCC, concordance correlation coefficient.
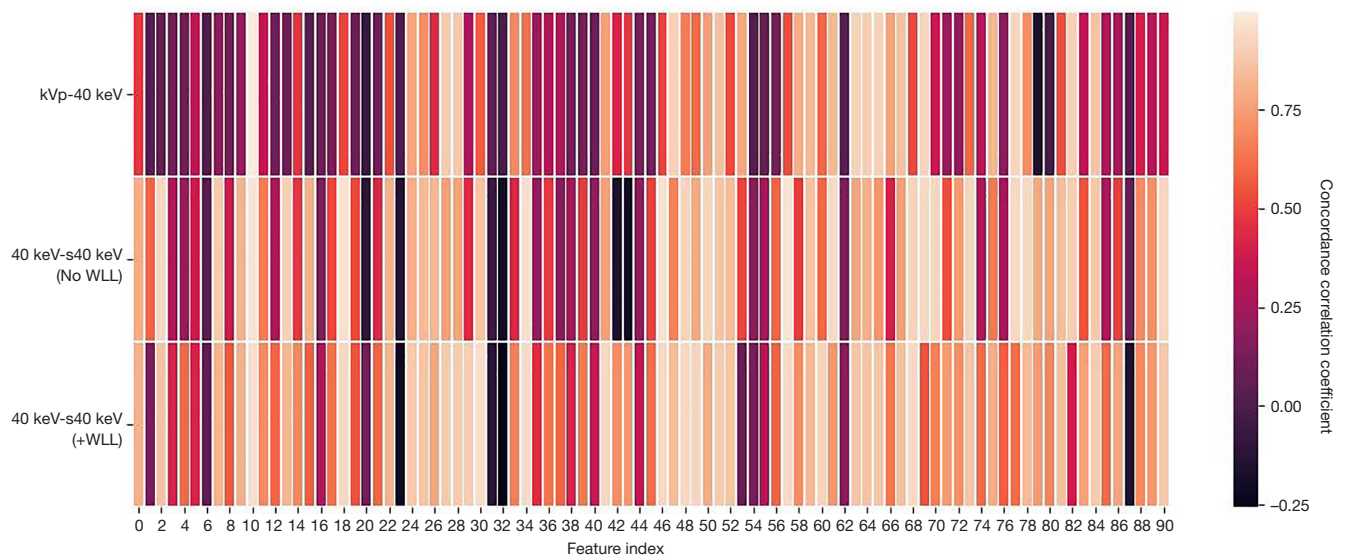
Figure 7 The heatmap shows the CCC comparison of radiomics features extracted from original images. Row 1 indicates the CCC between conventional CT images and virtual monoenergetic images. Row 2 indicates the CCC between synthetic virtual monoenergetic images using CycleGAN and virtual monoenergetic images. Row 3 indicates the CCC between synthetic VMIs using WLL-CycleGAN and virtual monoenergetic images. WLL, wavelet loss; CCC, concordance correlation coefficient; CT, computed tomography; GAN, generative adversarial network; VMIs, virtual monoenergetic images.

in GLDM at a threshold of 0.8. All methods performed worse than the baseline level in GLRLM and wavelet at a threshold of 0.8.

Discussion

Radiomic analysis has been widely applied to diagnosis and outcome prediction for cancers. Robustness and reproducibility of radiomic features is crucial in radiomics and has attracted the attention of researchers recently.

To address the issue of radiomics reproducibility, several compensation methods have been proposed to improve reproducibility of individual radiomics features (45,46). In contrast, the advantage of deep learning-based image synthesis is to work at an image level. This method can directly correct biases for original pixels. GAN-based deep learning methods are potential techniques for generating medical images from existing ones. Recently, many medical image translation studies have been reported: positron emission tomography (PET)-CT translation, correction of magnetic resonance motion artifacts, CBCT-to-CT translation, PET denoising, metal artifact reduction, and noise reduction from low dose CT (47-51).

In clinical practice, improved contrast attenuation with virtual monoenergetic (VM) imaging at lower kiloelectron volt levels enables better delineation and diagnostic accuracy in the detection of various vascular or oncologic abnormalities. Since providing more information of tissue than single polyenergetic image, monoenergetic images have been employed for radiomics analysis for diagnosis and outcome prediction recently (20-22).

The VMIs produced by DECT can provide different image contrasts: low energy (40–60 keV) for high soft tissue contrast and iodine attenuation; high energy (120–200 keV) to depress beam-hardening and metal artifacts (23-25). Therefore, different levels of VMIs obtained from 1 scan may provide different values of the same radiomics feature from conventional CT images. This facilitates the extraction of different dimensions of information from the same image, thus contributing to radiomics analysis. In other hand, data missing and inconsistency have become barriers in retrospective, longitudinal, or multicenter clinical studies. Deep learning-based image synthesis (translation or conversion) approaches may help to alleviate the above problems.

Conventional CT images, namely, kVp images, are reconstructed from the acquired project data by DECT devices using the conventional reconstruction algorithm.
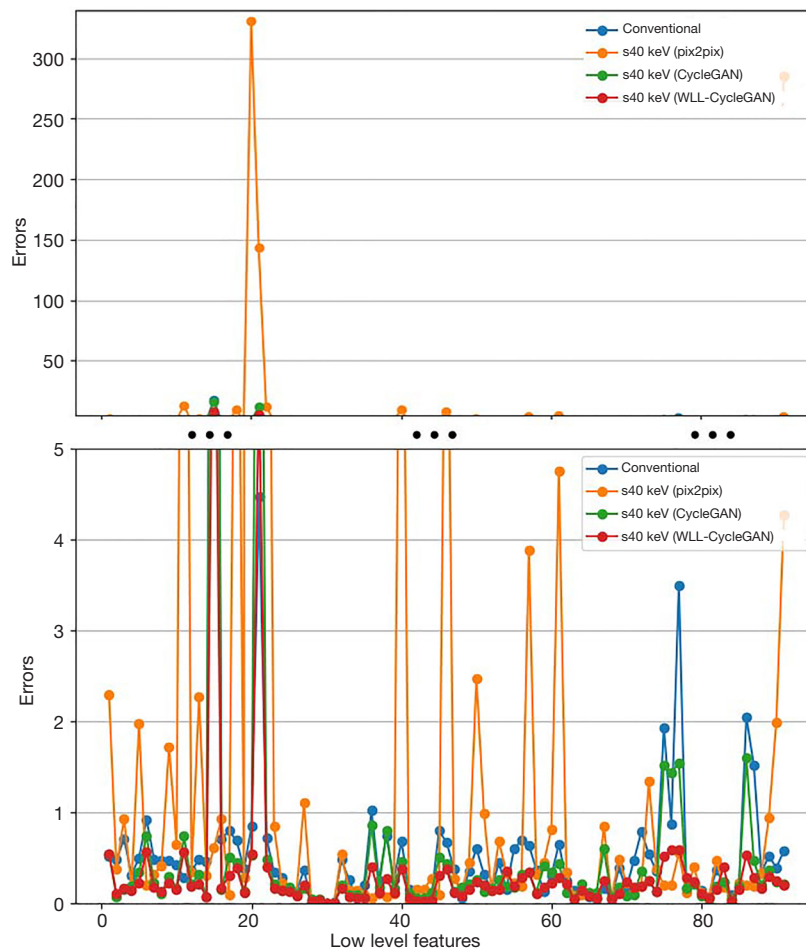
Figure 8 Comparison of errors in low-level texture features. Each line represents errors of radiomics features obtained from conventional CT images or synthetic VMIs and VMIs. s40 keV, synthetic 40 keV; GAN, generative adversarial network; WLL, wavelet loss; CT, computed tomography; VMIs, virtual monoenergetic images.
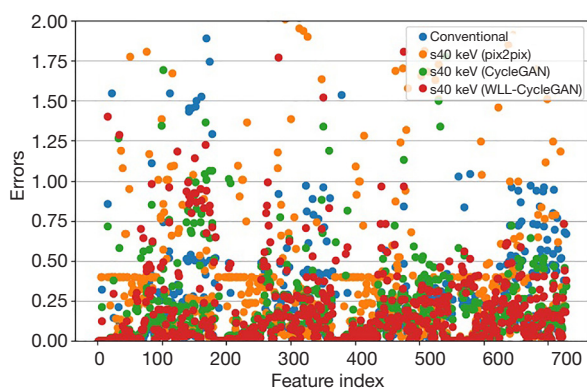
Figure 9 Comparison of errors in wavelet-based features. Each point represents errors of radiomics features obtained from conventional CT images or synthetic VMIs and VMIs. GAN, generative adversarial network; CT, computed tomography; WLL, wavelet loss; VMIs, virtual monoenergetic images.

Meanwhile, VMIs are reconstructed from the same project data using the reconstruction algorithm with material decomposition (34). Since the difference between conventional CT images and VMIs is generated by the reconstruction algorithm with material decomposition, different parameters will result in VMIs at varying energy levels.

All VMIs are reconstructed from one dual-energy project data by the 2-layer detector in the same way as the conventional CT image through material decomposition. Therefore, all VMIs and conventional CT images are pixel-wise consistent without position shift. The image registration is not necessary before feeding data into the network (23,52-54). Therefore, the CycleGAN-based model is suitable for these data since the paired reference images are ready-made.

Table 7 Image comparison with standard evaluation measures (from 40 keV to conventional CT image)

Comparison item	RMSE	PSNR	SSIM
40 keV *vs.* Conv image	54.75±11.9	12.94±2.1	0.625±8.3
sConv (pix2pix) *vs.* Conv image	47.80±41.9	31.17±6.4	0.703±3.1
sConv (CycleGAN) *vs.* Conv image	30.44±0.5	32.37±0.1	0.850±4.5
sConv (WLL-CycleGAN) *vs.* Conv image	23.66±0.5	34.56±0.2	0.894±2.3

Data format: mean ± standard deviation. CT, computed tomography; RMSE, root mean square error; PSNR, peak signal-to-noise ratio; SSIM, structure similarity index measure; sConv, synthetic conventional CT image; GAN, generative adversarial network; WLL, wavelet loss.
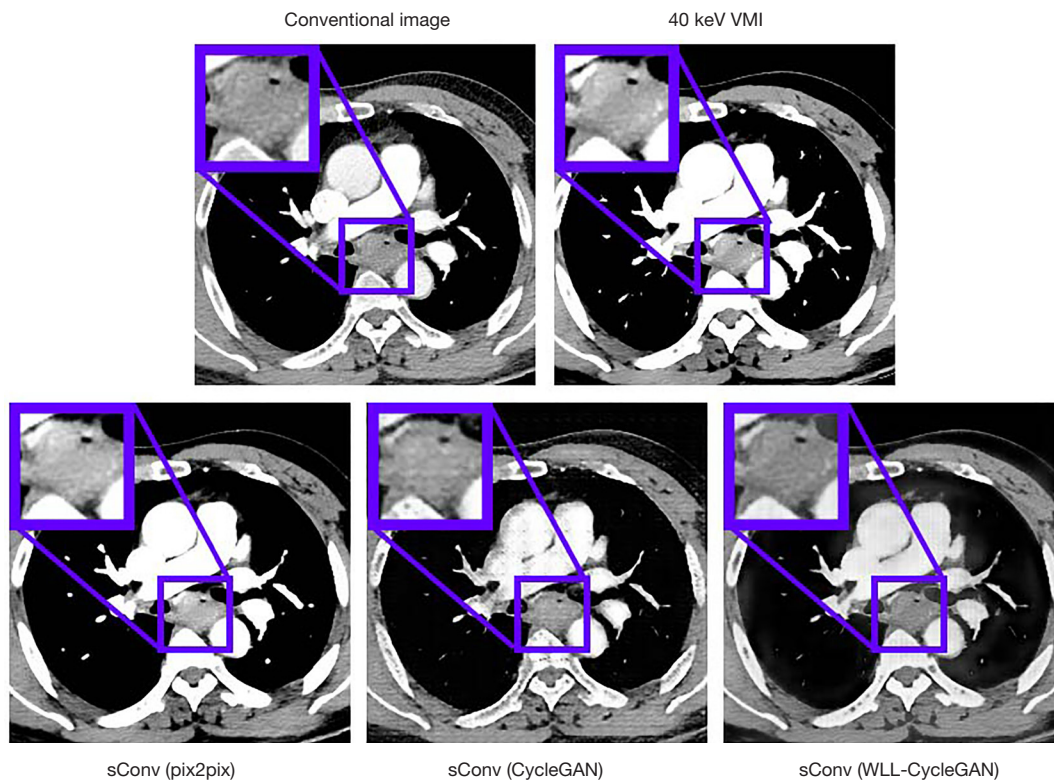
Figure 10 Image and ROI comparison: top row, column 1: conventional CT image; top row, column 2: 40 keV virtual monoenergetic image; bottom row, column 1: synthetic conventional CT image via pix2pix model; bottom row, column 2: synthetic conventional CT image via CycleGAN; bottom row, column 3: synthetic conventional CT image via proposed WLL-CycleGAN. All images are from the same slice of one patient. VMI, virtual monoenergetic image; sConv, synthetic conventional CT image; GAN, generative adversarial network; WLL, wavelet loss; ROI, region of interest; CT, computed tomography.

In this paper, we first investigated the impact of VMIs on radiomics features. The radiomics features extracted from both conventional CT images and VMIs were compared. Secondly, we defined the wavelet loss of 2 images to evaluate the high-frequency detailed differences. The proposed wavelet loss was incorporated into the CycleGAN model to synthesize VMIs from conventional CT images.

Finally, we evaluated the performance of image conversion using the proposed method and assessed whether it could improve the reproducibility of radiomic features between conventional CT images and VMIs.

Radiomics analysis can obtain internal features of images, whereas DWT can provide structure information of multi-level frequency in original images. The results
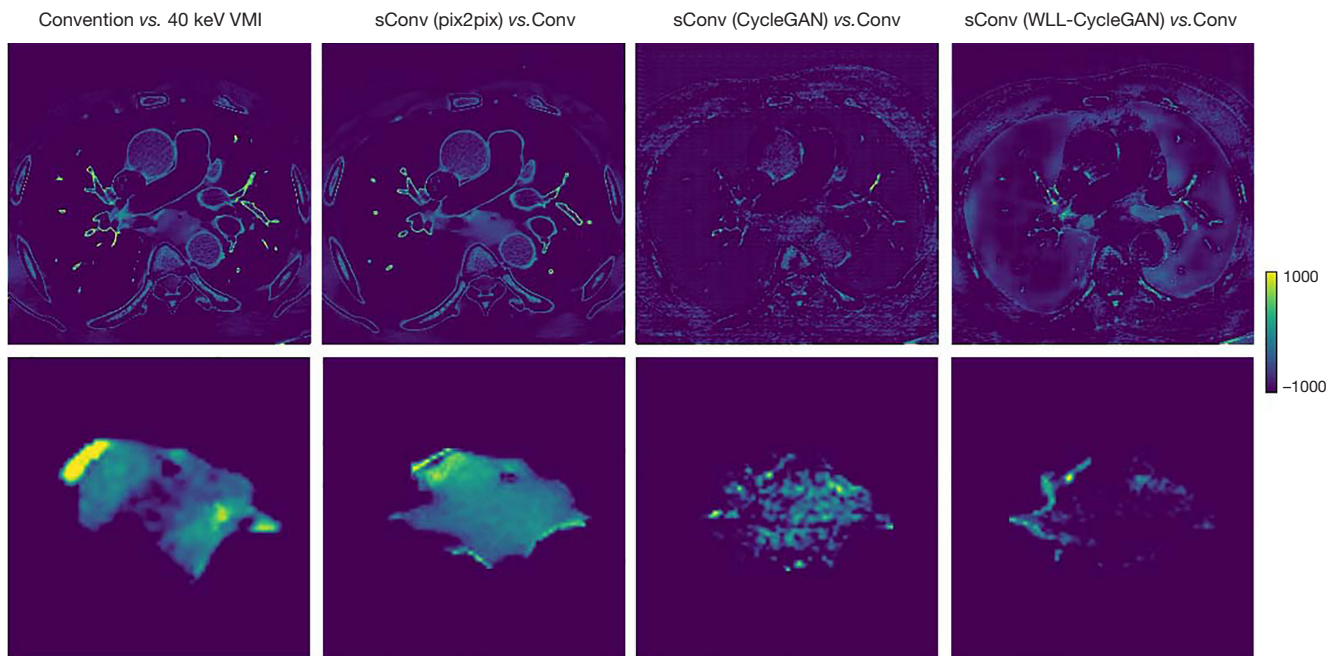
Figure 11 Comparison of image differences among all methods. The images represent the distinction between synthetic virtual monoenergetic images and the virtual monoenergetic images. Top row: whole body comparison; bottom row: ROI comparison. Column 1: the difference between conventional CT images and 40 keV VMI. Column 2: the difference between synthetic conventional CT images using pix2pix model and conventional CT images. Column 3: the difference between synthetic conventional CT images using CycleGAN and conventional CT images. Column 4: the difference between synthetic conventional CT images using proposed WLL-CycleGAN and conventional CT images. VMI, virtual monoenergetic image; sConv, synthetic conventional CT image; GAN, generative adversarial network; WLL, wavelet loss; ROI, region of interest; CT, computed tomography.
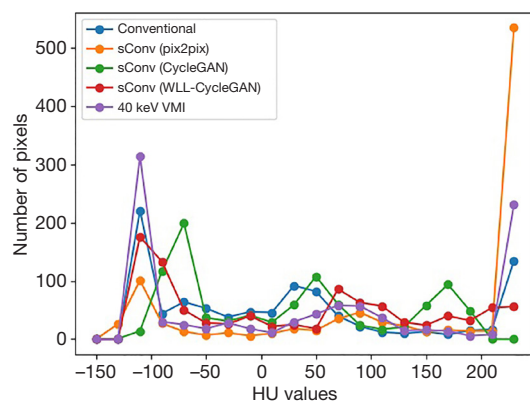
Figure 12 Histograms of HU values for each case for comparison (from 40 keV to conventional). sConv, synthetic conventional CT image; GAN, generative adversarial network; WLL, wavelet loss; VMI, virtual monoenergetic image; HU, Hounsfield unit; CT, computed tomography.

indicate that the proposed model reduces errors for 84% of low-level features, whereas the original CycleGAN reduces errors for 73% of low-level features, and the pix2pix model reduces errors for 20%. The proposed model reduces errors for 72% of wavelet features, whereas the original CycleGAN reduces errors for 40%, and the pix2pix model reduces errors for 6%. Due to the limitation of computational resource, a 2-dimensional (2D) network model and 2D-DWT were employed for image translating. With the improvement of the image quality of each slice, the robustness of 3D radiomics features are improved. In the future, we can try to use a 3D network model with 3D-DWT to translate image blocks directly.

Although the CycleGAN network was originally designed for unpaired data and unsupervised learning tasks, in several studies, training images are still paired by registration to preserve quantitative pixel values and remove

Table 8 Quantitative Metrics of Intensity histogram (from 40 keV to conventional)

|	Conventional *vs.* VMI	sConv VMI pix2pix	sConv VMI CycleGAN	sConv VMI WLL-CycleGAN
RMSE	58.59	98.71	70.16	42.04

VMI, virtual monoenergetic image; sConv, synthetic conventional CT image; GAN, generative adversarial network; WLL, wavelet loss; CT, computed tomography; RMSE, root mean square errors.
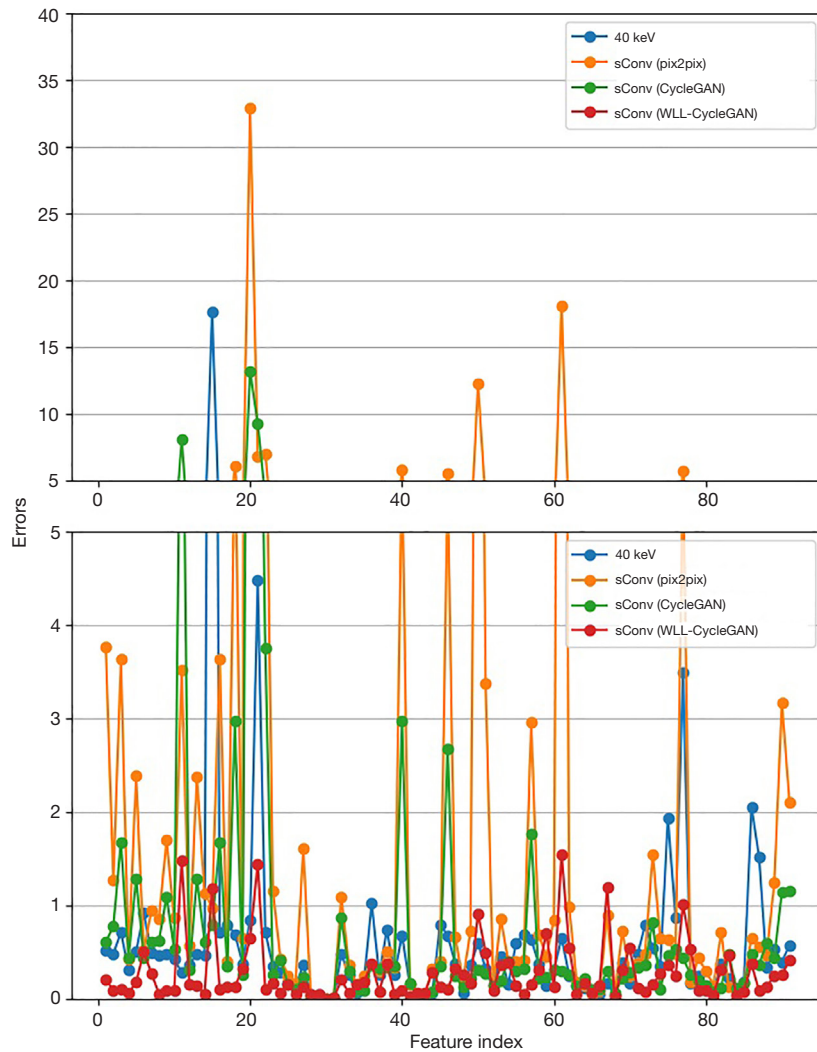
Figure 13 Error comparison of low-level texture features for the synthesis from 40 keV VMI to conventional CT images (from 40 keV to conventional). sConv, synthetic conventional CT image; GAN, generative adversarial network; WLL, wavelet loss; VMI, virtual monoenergetic image; CT, computed tomography.

large geometric mismatch to allow the network to focus on mapping details and accelerate training (32,55). Due to the inverse path favoring a one-to-one correspondence between the input and output, the training of the GAN is less affected by mode collapse (55). The cycle consistency may help to reduce the space of possible mapping functions and allows for higher accuracy because the model is doubly constrained (31,32). The above reasons may help to understand the result that the CycleGAN-based model
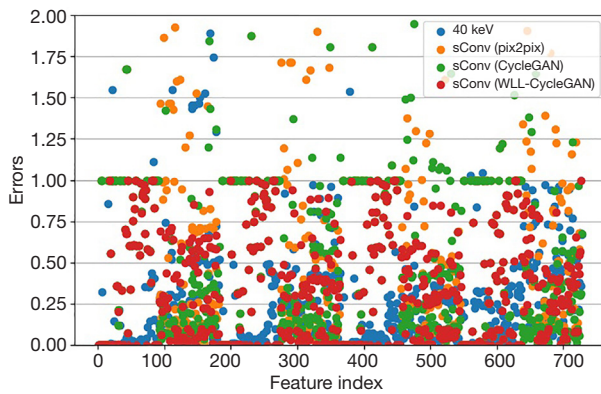
Figure 14 Error comparison of wavelet-based features (from 40 keV to conventional). sConv, synthetic conventional CT image; GAN, generative adversarial network; WLL, wavelet loss; CT, computed tomography.

outperforms pix2pix-GAN model.

As shown in *Figures 4,5*, CycleGAN produces artifacts in synthetic images such as streaking lines, possibly due to the cyclic loss term and some form of mode collapse. Our proposed WLL-CycleGAN method avoids these artifacts by incorporating paired loss terms in addition to the cycle-consistency loss.

There are a few of limitations of this work. First, only the dual-layer spectral DECT of 1 manufacturer (Philips) was considered. Different mechanisms for obtaining VMIs may affect the reproducibility of radiomics features, and the influence should be studied. Second, only the conversion between conventional CT images and VMIs were performed. In the future, the performance for improving radiomics features' reproducibility of deep learning models translating CT images at any monoenergetic level to another can be evaluated. Third, the effectiveness of the deep learning model for improving radiomics features was validated through only value errors and CCC. The actual effect of synthetic images for radiomics analysis tasks, such as disease prognosis and outcome prediction, should be evaluated.

In the future, we can also investigate the performance of the deep learning model for improving radiomics feature reproducibility in other types of images, such as multi-sequence MRI or PET. We can extend our proposed wavelet-based loss paired CycleGAN to a 3D model.

Table 9 Number of radiomic features meeting criteria of reproducibility before and after image conversion (from 40 keV to conventional)

Feature class	Conv-40 keV		Conv-sConv (pix2pix)		Conv-sConv (CycleGAN)		Conv-sConv (WLL-CycleGAN)	
	0.8	0.85	0.8	0.85	0.8	0.85	0.8	0.85
First order	1 [5.6]	1 [5.6]	2 [11.1]	2 [11.1]	1 [5.6]	1 [5.5]	8 [44.4]	6 [33.3]
GLCM	2 [9]	2 [9]	3 [13.6]	2 [9]	3 [13.6]	1 [4.5]	7 [31.8]	4 [18.2]
GLDM	2 [14.3]	2 [14.3]	2 [14.3]	2 [14.3]	6 [42.9]	4 [28.6]	4 [28.6]	3 [21.4]
GLRLM	8 [50]	5 [31.2]	4 [25]	4 [25]	3 [18.8]	3 [18.8]	5 [31.2]	5 [31.3]
GLSZM	4 [25]	3 [18.8]	4 [25]	4 [25]	4 [25]	3 [18.8]	7 [43.8]	6 [37.5]
NGTDM	0 [0]	0 [0]	0[0]	0[0]	1 [20]	0 [0]	2 [40]	0 [0]
Wavelet	268 [36.8]	225 [31]	20 [8]	13 [6]	212 [30]	196 [26.9]	249 [34.2]	229 [1.5]

(I) Numbers are count of radiomic features. Numbers in square brackets are percentages; (II) CCC are used as thresholds. sConv, synthetic conventional CT images; GAN, generative adversarial network; WLL, wavelet loss; GLCM, gray level co-occurrence matrix; GLDM, gray-level difference matrix; GLRLM, gray-level run-length matrix; GLSZM, gray-level size-zone matrix; NGTDM, neighborhood gray-tone difference matrix; CCC, concordance correlation coefficient; CT, computed tomography.

Conclusions

In this paper, we first explored the reproducibility of radiomic features extracted from conventional CT images and VMIs. The results indicated that radiomics features obtained from VMIs may differ from those obtained from conventional CT images. Secondly, by exploiting the wavelet loss to evaluate the high-frequency detailed differences, the WLL-CycleGAN based deep learning method was developed to translate conventional CT images to VMIs for improving the reproducibility of radiomics features. Our proposed method was shown to be effective for this addressing issue. Compared to pix2pix and CycleGAN, our proposed WLL-CycleGAN produced better performance.

Acknowledgments

Footnote

Conflicts of Interest: All authors have completed the ICMJE uniform disclosure form (available at https://qims.amegroups.com/article/view/10.21037/qims-23-922/coif). The authors have no conflicts of interest to declare.

Ethical Statement: The authors are accountable for all aspects of the work in ensuring that questions related to the accuracy or integrity of any part of the work are appropriately investigated and resolved. The study was conducted in accordance with the Declaration of Helsinki (as revised in 2013). The study was approved by the Ethics Committee of Shandong Cancer Hospital and Institute, and the requirement for individual consent for this retrospective analysis was waived.

References

1. Gillies RJ, Kinahan PE, Hricak H. Radiomics: Images Are More than Pictures, They Are Data. Radiology 2016;278:563-77.

2. Lambin P, Rios-Velazquez E, Leijenaar R, Carvalho S, van Stiphout RG, Granton P, Zegers CM, Gillies R, Boellard R, Dekker A, Aerts HJ. Radiomics: extracting more information from medical images using advanced feature analysis. Eur J Cancer 2012;48:441-6.

3. Kumar V, Gu Y, Basu S, Berglund A, Eschrich SA, Schabath MB, Forster K, Aerts HJ, Dekker A, Fenstermacher D, Goldgof DB, Hall LO, Lambin P, Balagurunathan Y, Gatenby RA, Gillies RJ. Radiomics: the process and the challenges. Magn Reson Imaging 2012;30:1234-48.

4. Nie K, Al-Hallaq H, Li XA, Benedict SH, Sohn JW, Moran JM, Fan Y, Huang M, Knopp MV, Michalski JM, Monroe J, Obcemea C, Tsien CI, Solberg T, Wu J, Xia P, Xiao Y, El Naqa I. NCTN Assessment on Current Applications of Radiomics in Oncology. Int J Radiat Oncol Biol Phys 2019;104:302-15.

5. Touati R, Le WT, Kadoury S. A feature invariant generative adversarial network for head and neck MRI/CT image synthesis. Phys Med Biol 2021. doi: 10.1088/1361-6560/abf1bb.

6. Dalmaz O, Yurt M, Cukur T. ResViT: Residual Vision Transformers for Multimodal Medical Image Synthesis. IEEE Trans Med Imaging 2022;41:2598-614.

7. Touati R, Kadoury S. Bidirectional feature matching based on deep pairwise contrastive learning for multiparametric MRI image synthesis. Phys Med Biol 2023. doi: 10.1088/1361-6560/acda78.

8. Touati R, Kadoury S. A least square generative network based on invariant contrastive feature pair learning for multimodal MR image synthesis. Int J Comput Assist

2388

Xu et al. CycleGAN method for improving radiomics features robustness

Radiol Surg 2023;18:971-9.

9. Shan H, Padole A, Homayounieh F, Kruger U, Khera RD, Nitiwarangkul C, Kalra MK, Wang G. Competitive performance of a modularized deep neural network compared to commercial algorithms for low-dose CT image reconstruction. Nat Mach Intell 2019;1:269-76.

10. Kyong Hwan Jin, McCann MT, Froustey E, Unser M. Deep Convolutional Neural Network for Inverse Problems in Imaging. IEEE Trans Image Process 2017;26:4509-22.

11. Zhao T, McNitt-Gray M, Ruan D. A convolutional neural network for ultra-low-dose CT denoising and emphysema screening. Med Phys 2019;46:3941-50.

12. Traverso A, Wee L, Dekker A, Gillies R. Repeatability and Reproducibility of Radiomic Features: A Systematic Review. Int J Radiat Oncol Biol Phys 2018;102:1143-58.

13. Jahanshahi A, Soleymani Y, Fazel Ghaziani M, Khezerloo D. Radiomics reproducibility challenge in computed tomography imaging as a nuisance to clinical generalization: a mini-review. Egypt J Radiol Nucl Med 2023;83:54.

14. Choe J, Lee SM, Do KH, Lee G, Lee JG, Lee SM, Seo JB. Deep Learning-based Image Conversion of CT Reconstruction Kernels Improves Radiomics Reproducibility for Pulmonary Nodules or Masses. Radiology 2019;292:365-73.

15. Marcadent S, Hofmeister J, Preti MG, Martin SP, Van De Ville D, Montet X. Generative Adversarial Networks Improve the Reproducibility and Discriminative Power of Radiomic Features. Radiol Artif Intell 2020;2:e190035.

16. Li Y, Han G, Wu X, Li ZH, Zhao K, Zhang Z, Liu Z, Liang C. Normalization of multicenter CT radiomics by a generative adversarial network method. Phys Med Biol 2021. doi: 10.1088/1361-6560/ab8319.

17. Zhang Z, Huang M, Jiang Z, Chang Y, Torok J, Yin FF, Ren L. 4D radiomics: impact of 4D-CBCT image quality on radiomic analysis. Phys Med Biol 2021;66:045023.

18. Park S, Lee SM, Do KH, Lee JG, Bae W, Park H, Jung KH, Seo JB. Deep Learning Algorithm for Reducing CT Slice Thickness: Effect on Reproducibility of Radiomic Features in Lung Cancer. Korean J Radiol 2019;20:1431-40.

19. Booz C, Nöske J, Martin SS, Albrecht MH, Yel I, Lenga L, Gruber-Rouh T, Eichler K, D'Angelo T, Vogl TJ, Wichmann JL. Virtual Noncalcium Dual-Energy CT: Detection of Lumbar Disk Herniation in Comparison with Standard Gray-scale CT. Radiology 2019;290:446-55.

20. Euler A, Laqua FC, Cester D, Lohaus N, Sartoretti T, Pinto Dos Santos D, Alkadhi H, Baessler B. Virtual Monoenergetic Images of Dual-Energy CT-Impact on Repeatability, Reproducibility, and Classification in Radiomics. Cancers (Basel) 2021;13:4710.

21. Han D, Yu Y, He T, Yu N, Dang S, Wu H, Ren J, Duan X. Effect of radiomics from different virtual monochromatic images in dual-energy spectral CT on the WHO/ISUP classification of clear cell renal cell carcinoma. Clin Radiol 2021;76:627.e23-627.e29.

22. An C, Li D, Li S, Li W, Tong T, Liu L, Jiang D, Jiang L, Ruan G, Hai N, Fu Y, Wang K, Zhuo S, Tian J. Deep learning radiomics of dual-energy computed tomography for predicting lymph node metastases of pancreatic ductal adenocarcinoma. Eur J Nucl Med Mol Imaging 2022;49:1187-99.

23. Albrecht MH, Vogl TJ, Martin SS, Nance JW, Duguay TM, Wichmann JL, De Cecco CN, Varga-Szemes A, van Assen M, Tesche C, Schoepf UJ. Review of Clinical Applications for Virtual Monoenergetic Dual-Energy CT. Radiology 2019;293:260-71.

24. Siegel MJ, Kaza RK, Bolus DN, Boll DT, Rofsky NM, De Cecco CN, Foley WD, Morgan DE, Schoepf UJ, Sahani DV, Shuman WP, Vrtiska TJ, Yeh BM, Berland LL. White Paper of the Society of Computed Body Tomography and Magnetic Resonance on Dual-Energy CT, Part 1: Technology and Terminology. J Comput Assist Tomogr 2016;40:841-5.

25. Paganetti H, Beltran C, Both S, Dong L, Flanz J, Furutani K, Grassberger C, Grosshans DR, Knopf AC, Langendijk JA, Nystrom H, Parodi K, Raaymakers BW, Richter C, Sawakuchi GO, Schippers M, Shaitelman SF, Teo BKK, Unkelbach J, Wohlfahrt P, Lomax T. Roadmap: proton therapy physics and biology. Phys Med Biol 2021. doi: 10.1088/1361-6560/abcd16.

26. Cong W, Xi Y, Fitzgerald P, De Man B, Wang G. Virtual Monoenergetic CT Imaging via Deep Learning. Patterns (N Y) 2020;1:100128.

27. Funama Y, Oda S, Kidoh M, Nagayama Y, Goto M, Sakabe D, Nakaura T. Conditional generative adversarial networks to generate pseudo low monoenergetic CT image from a single-tube voltage CT scanner. Phys Med 2021;83:46-51.

28. Kawahara D, Saito A, Ozawa S, Nagata Y. Image synthesis with deep convolutional generative adversarial networks for material decomposition in dual-energy CT from a kilovoltage CT. Comput Biol Med 2021;128:104111.

29. Lyu T, Zhao W, Zhu Y, Wu Z, Zhang Y, Chen Y, Luo L, Li S, Xing L. Estimating dual-energy CT imaging from single-energy CT data with material decomposition convolutional neural network. Med Image Anal 2021;70:102001.

30. Kikinis R, Pieper SD, Vosburgh KG. 3D Slicer: A Platform for Subject-Specific Image Analysis, Visualization, and Clinical Support. In: Jolesz F. editor. Intraoperative Imaging and Image-Guided Therapy. Springer, New York, NY, 2024.

31. Zhu JY, Park T, Isola P, Efros AA. Unpaired image-to-image translation using cycle-consistent adversarial networks. IEEE International Conference on Computer Vision (ICCV), Venice, Italy, 2017:2223-32.

32. Harms J, Lei Y, Wang T, Zhang R, Zhou J, Tang X, Curran WJ, Liu T, Yang X. Paired cycle-GAN-based image correction for quantitative cone-beam computed tomography. Med Phys 2019;46:3998-4009.

33. Liu Y, Lei Y, Wang T, Fu Y, Tang X, Curran WJ, Liu T, Patel P, Yang X. CBCT-based synthetic CT generation using deep-attention cycleGAN for pancreatic adaptive radiotherapy. Med Phys 2020;47:2472-83.

34. Philips, "Philips Healthcare Spectral CT." 2023. Available online: https://www.philips.com.tw/healthcare/sites/spectral-ct-learning-center

35. Chen KM. Principles and clinical applications of spectral CT imaging. Science 2012. (in Chinese). Available online: https://book.sciencereading.cn/shop/book/Booksimple/show.do?id=B9759E7063FB34D34A47A514F466D5789000

36. Johnson TR. Dual-energy CT: general principles. AJR Am J Roentgenol 2012;199:S3-8.

37. P. S. Foundation, Python, 2021. Available online: https://www.python.org

38. Google, Tensorflow, 2021. Available online: https://www.tensorflow.org

39. Pyradiomics, 2020. Available online: https://www.radiomics.io/pyradiomics.html

40. Haralick RM, Shanmugam K, Dinstein IH. Textural features for image classification. IEEE Transactions on Systems, Man, and Cybernetics 1973;6:610-21.

41. Galloway MM. Texture analysis using grey level run lengths. STIN 1974;75:18555.

42. Thibault G, Angulo J, Meyer F. Advanced statistical matrices for texture characterization: application to cell classification. IEEE Trans Biomed Eng 2014;61:630-7.

43. Amadasun M, King R. Textural features corresponding to textural properties. IEEE Transactions on Systems, Man, and Cybernetics 1989;19:1264-74.

44. Isola P, Zhu JY, Zhou T, Efros AA. Image-to-image translation with conditional adversarial networks. IEEE Conference on Computer Vision and Pattern Recognition (CVPR), Honolulu, HI, USA, 2017:1125-34.

45. O'Connor JP, Aboagye EO, Adams JE, Aerts HJ, Barrington SF, Beer AJ, et al. Imaging biomarker roadmap for cancer studies. Nat Rev Clin Oncol 2017;14:169-86.

46. Orlhac F, Boughdad S, Philippe C, Stalla-Bourdillon H, Nioche C, Champion L, Soussan M, Frouin F, Frouin V, Buvat I. A Postreconstruction Harmonization Method for Multicenter Radiomic Studies in PET. J Nucl Med 2018;59:1321-8.

47. Yi X, Walia E, Babyn P. Generative adversarial network in medical imaging: A review. Med Image Anal 2019;58:101552.

48. Dar SU, Yurt M, Karacan L, Erdem A, Erdem E, Cukur T. Image Synthesis in Multi-Contrast MRI With Conditional Generative Adversarial Networks. IEEE Trans Med Imaging 2019;38:2375-88.

49. Armanious K, Jiang C, Fischer M, Küstner T, Hepp T, Nikolaou K, Gatidis S, Yang B. MedGAN: Medical image translation using GANs. Comput Med Imaging Graph 2020;79:101684.

50. Chen L, Liang X, Shen C, Nguyen D, Jiang S, Wang J. Synthetic CT generation from CBCT images via unsupervised deep learning. Phys Med Biol 2021. doi: 10.1088/1361-6560/ac01b6.

51. Zhang Y, Yue N, Su MY, Liu B, Ding Y, Zhou Y, Wang H, Kuang Y, Nie K. Improving CBCT quality to CT level using deep learning with generative adversarial network. Med Phys 2021;48:2816-26.

52. Grant KL, Flohr TG, Krauss B, Sedlmair M, Thomas C, Schmidt B. Assessment of an advanced image-based technique to calculate virtual monoenergetic computed tomographic images from a dual-energy examination to improve contrast-to-noise ratio in examinations using iodinated contrast media. Invest Radiol 2014;49:586-92.

53. Albrecht MH, Trommer J, Wichmann JL, Scholtz JE, Martin SS, Lehnert T, Vogl TJ, Bodelle B. Comprehensive Comparison of Virtual Monoenergetic and Linearly Blended Reconstruction Techniques in Third-Generation Dual-Source Dual-Energy Computed Tomography Angiography of the Thorax and Abdomen. Invest Radiol 2016;51:582-90.

54. Albrecht MH, Scholtz JE, Hüsers K, Beeres M, Bucher AM, Kaup M, Martin SS, Fischer S, Bodelle B, Bauer RW, Lehnert T, Vogl TJ, Wichmann JL. Advanced image-based virtual monoenergetic dual-energy CT angiography of the abdomen: optimization of kiloelectron volt settings to improve image contrast. Eur Radiol 2016;26:1863-70.

55. Zhou L, Schaefferkoetter JD, Tham IWK, Huang G, Yan J. Supervised learning with cyclegan for low-dose FDG PET image denoising. Med Image Anal 2020;65:101770.